JNeurosci
THE JOURNAL OF NEUROSCIENCE

Research Articles | Cellular/Molecular

# Widely used CaMKII regulatory segment mutations cause tight actinin binding and dendritic spine enlargement in unstimulated neurons

https://doi.org/10.1523/JNEUROSCI.0795-25.2025

Received: 22 April 2025
Revised: 13 September 2025
Accepted: 17 September 2025

# Widely used CaMKII regulatory segment mutations cause tight actinin binding and dendritic spine enlargement in unstimulated neurons

Running title: Tight actinin binding in a common CaMKII variant

Ashton J. Curtis[a]*, Jian Zhu[a]*, Dorota Studniarczyk[a], Timothy W. Church[a], Mark Farrant[a], Matthew G. Gold[a,1]

[a]Department of Neuroscience, Physiology and Pharmacology, University College London, Gower Street, LONDON, WC1E 6BT, UK

*These authors contributed equally

[1]Correspondence: m.gold@ucl.ac.uk

*Word counts*

Abstract: 247 words (250 max)

Significance statement: 120 words (120 max)

Introduction: 650 words (650 max)

Discussion: 1488 words (1500 max)

**Conflict of interest statement**

The authors declare no competing interest.

## Abstract

$Ca^{2+}$/calmodulin-dependent protein kinase II (CaMKII) is essential for long-term potentiation (LTP) of excitatory synapses, a process fundamental to learning. CaMKII responds to $Ca^{2+}$ influx into postsynaptic spines by phosphorylating proteins and forming new protein interactions. The relative importance of these enzymatic and structural functions is debated. LTP induction triggers CaMKII docking to NMDA receptors, and recent evidence indicates that LTP can proceed without kinase activity after this event. Furthermore, interactions between CaMKII and α-actinin-2 that form following LTP induction are required for dendritic spine enlargement. CaMKII can auto-phosphorylate at T286, which enables autonomous activity after $Ca^{2+}$/CaM dissociation. Experiments with CaMKII variants including a T305A/T306A ('AA') double substitution have led to a model whereby T305/T306 phosphorylation by autonomously active CaMKII prevents further $Ca^{2+}$/CaM activation. However, this mechanism is not fully compatible with previous studies including a phospho-proteomic analysis of CaMKII and imaging using CaMKII activity reporters in live neurons. In this study, we show using rat hippocampal cultures that the AA substitution has an unintended gain-of-function property: elevated binding to α-actinin-2 in unstimulated neurons to a level only normally observed after induction of LTP. CaMKIIα AA also increases the proportion of enlarged spines in unstimulated neurons without altering synaptic currents. Calorimetric measurements with purified protein confirm that α-actinin-2 binds tightly to CaMKIIα AA with no requirement for kinase activation. Using x-ray crystallography, we show that the AA substitution enables α-actinin-2 to adopt a different tighter binding mode. Our findings reinforce the notion that CaMKII primarily fulfils a structural role in LTP.

## Significance statement

New memories are encoded in the brain by long-lasting changes in the strength of neuronal synapses. The most common form of synaptic strengthening is driven by the abundant calcium-sensitive enzyme CaMKII. Most research has focused on CaMKII phosphorylation of proteins including itself with the assumption that such enzymatic activity is key to its ability to strengthen synapses. However, it is becoming apparent that formation of protein-protein interactions involving CaMKII is more critical. Here, we show that two mutations commonly used to prevent auto-phosphorylation in a regulatory region of CaMKII have an unexpected gain-of-function property: they trigger tight binding to an actin crosslinking protein leading to synaptic enlargement. Our study supports the idea that CaMKII acts primarily as a structural protein.

## Introduction

Changes in the strength of synapses are fundamental to encoding new memories and behavioural adaptations (Takeuchi et al., 2014). In excitatory glutamatergic synapses, large $Ca^{2+}$ influxes through postsynaptic NMDA receptors (NMDARs) trigger long-lasting changes in the size and responsiveness of dendritic spines known as long-term potentiation (LTP) (Anggono and Huganir, 2012). $Ca^{2+}$/calmodulin (CaM)-dependent protein kinase II (CaMKII) is essential for sensing $Ca^{2+}$ influx (Hell, 2014). In response to $Ca^{2+}$/CaM activation, CaMKII phosphorylates receptors and structural proteins, and forms new protein-protein interactions that result in the full expression of LTP including reorganisation of the actin cytoskeleton into enlarged mushroom-shaped spines (Hell, 2014). Recent studies suggest that the latter structural function may be more critical (Tullis et al., 2023).

Many studies have focused on understanding how CaMKII activity is regulated by autophosphorylation at positions T286, T305 and T306 (**Fig. 1a**). Inter-subunit phosphorylation at T286 generates an autonomously-active state that retains some activity after $Ca^{2+}$/CaM dissociation (Miller et al., 1988; Schworer et al., 1988; Thiel et al., 1988). However, more recent measurements in live neurons using CaMKII activity reporters indicate that such phosphorylation only endures for seconds after the $Ca^{2+}$ impulse has receded (Chang et al., 2017; Yasuda et al., 2022). Threonines 305 and 306 fall within the regulatory segment (**Fig. 1a**). It is widely thought that autonomously-active CaMKII can phosphorylate these sites to prevent subsequent $Ca^{2+}$/CaM activation (Hanson and Schulman, 1992). Many studies have employed the double alanine substitution T305A/T306A (referred to as 'AA' hereafter), with the aim of preventing this proposed inhibitory phosphorylation. The AA substitution greatly slows the rate of CaMKIIα dissociation from synapses (Shen et al., 2000). The AA substitution is often combined with a T286D substitution – expression of this CaMKII triple mutant generates highly potentiated synapses that are not amenable to LTD (Pi et al., 2010b; Pi et al., 2010a; Incontro et al., 2018). However, quantitative proteomics indicates that CaMKII cannot efficiently phosphorylate T305 and T306 (Baucum et al., 2015), and imaging with CaMKII conformation reporters shows that T286D substitution alone does not markedly affect the ability of $Ca^{2+}$/CaM to activate the enzyme (Chang et al., 2017). A possible explanation is that the CaMKII regulatory segment is also important for mediating interactions with α-actinin-2.

A structural role for CaMKII was posited as soon as its neuronal abundance became apparent (Erondu and Kennedy, 1985). CaMKII forms dodecamers with three domains per protomer capable of protein interactions (Myers et al., 2017; Penny and Gold, 2018). CaMKII docking to NMDARs has emerged as a key initial step that occurs within the first ~15 seconds of LTP induction (Yasuda et al., 2022). After $Ca^{2+}$/CaM binds to the regulatory segment of CaMKII, a substrate motif in the GluN2B subunit tail is able to access the substrate-binding groove of the CaMKII kinase domain (Ozden et al., 2022). The resulting complex is highly stable (Bayer et al., 2001). Experiments with a CaMKII inhibitor that doesn't affect its ability to bind NMDARs show that, remarkably, CaMKII kinase activity is dispensable for LTP elicited by robust stimuli (Tullis et al., 2023) – its structural capabilities are sufficient. 'Follower'-type CaMKII interactions have been hypothesised as a means to translate the initial cue provided by CaMKII docking to NMDARs into the full structural and functional changes that occur in LTP (Yasuda et al., 2022). We recently discovered one such interaction that forms between CaMKII and the actin crosslinking protein α-actinin-2 within ~1-2 minutes of the $Ca^{2+}$ impulse (Curtis et al., 2023). α-actinin-2 can bind both CaMKIIα and CaMKIIβ (Robison et al., 2005). Association of CaMKII with GluN2B subunits releases the regulatory segment from the kinase domain, which enables higher affinity binding to the third and fourth EF hands (EF3-4) of α-actinin-2 (Curtis et al., 2023). This likely explains why α-actinin-2 binding 'follows' initial docking to NMDARs (Saneyoshi, 2023). In this study we explored the idea that the AA substitution might act at least in part by providing a 'shortcut' to this elevated interaction between α-actinin-2 and CaMKII.

## Materials and Methods

### Protein expression and purification

Human α-actinin-2 EF3-4 (positions 827-894) was expressed with an N-terminal Tev-cleavable His-GST tag within pET28. Protein expression was induced in Rosetta plysS *E. coli* with 1 mM IPTG, and cells were harvested after overnight incubation at 20 °C. Cells were lysed in Ni-NTA buffer A (500 mM NaCl, 25 mM Tris pH 8, 1 mM Benzamidine, 30 mM imidazole) supplemented with 0.1 mg/mL lysozyme and one cOmplete protease inhibitor tablet per 100 mL, then clarified by high-speed centrifugation following sonication. His-GST-EF3-4 was enriched by sequential Ni-NTA agarose (Qiagen) and Glutathione Sepharose 4B (Cytiva) affinity capture as before (Curtis et al., 2023) prior to overnight cleavage with Tev protease at 4 °C. Finally, EF3-4 was resolved from cleaved GST using a HiLoad 16/600 Superdex 75 column equilibrated in 20 mM HEPES, pH 7.5, 0.15 M NaCl, and 1 mM DTT. CaMKIIα 1-315 variants were expressed with Tev-cleavable N-terminal His-Trx tag in Rosetta (DE3) pLysS *E. coli* (Merck) using pNH-TrxT vector as before (Curtis et al., 2023). Alanine substitutions at positions T305 and T306 were introduced by site directed mutagenesis using primers listed in **supplemental Table S4**. Trx-CaMKII construct expression was induced with 0.2 mM IPTG, with cells harvested after overnight incubation at 18 °C. Initial purification was performed by affinity to Ni-NTA agarose and anion exchange with Q Fast Flow columns (Cytiva) as before (Curtis et al., 2023). We found that if the Trx moiety was removed by Tev cleavage, CaMKIIα 1-315 was prone to precipitate unless bound to EF3-4. Therefore, different purification strategies were adopted for crystallography and ITC. For ITC measurements, the Trx tag was retained, and Trx-CaMKIIα was immediately subjected to size exclusion with a HiLoad Superdex 75 column (Cytiva) equilibrated in gel filtration buffer (20 mM HEPES pH 7.5, 150 mM NaCl, 1 mM DTT) following anion exchange. For crystallisation of the complex, the His-Trx-CaMKIIα AA 1-315 construct was mixed with a two-fold molar excess of EF3-4 for one hour, before addition of Tev protease. The complex was then resolved from excess EF3-4 and Trx using the same size exclusion approach on the following day. All protein samples were concentrated using 10K MWCO centrifugal concentrators (Sartorius). Dialysis was performed using Slide-a-Lyzer 2K MWCO cassettes (Thermo Scientific).

**Crystallography**. For crystallisation of CaMKIIα 1-315 AA in complex with α-actinin-2 EF3-4, the CaMKII construct was first mixed with a ~2-fold molar excess of EF3-4 before the 1:1 complex was separated from excess EF3-4 using size exclusion with a Superdex 75 column equilibrated in 20 mM HEPES, pH 7.5, 0.15 M NaCl, 1 mM DTT. The complex was concentrated to 10 mg/mL and crystals were grown using sitting drop vapor diffusion with precipitant solution containing 0.2 M Lithium sulfate, 0.1 M MES pH 6.0, 20 % w/v PEG 4000. For crystals containing ADP or AMP-PNP, the precipitant solution was supplemented with 10 mM $MgCl_2$ and 5 mM nucleotide. Diffraction data were collected at Diamond Light Source beamline I24 and reduced using DIALS (Winter et al., 2018), before scaling with Aimless (Evans and Murshudov, 2013). The structures were solved by molecular replacement using Phaser (McCoy et al., 2007), and finally refined in PHENIX (Liebschner et al., 2019). Full data collection and refinement statistics are provided in **supplemental Table S3**. Structural alignments and RMSD calculations were performed using GESAMT (Krissinel, 2012).

**Kinase assays**. CaMKII kinase assays were performed using the ADP-Glo (Promega) detection system to monitor conversion of ATP to ADP upon syntide-2 phosphorylation. Assays were performed using full-length mouse His-CaMKIIα variants purified after expression in HEK293T cells (Curtis et al., 2023). Assays were performed with 300 μM syntide-2 (Genscript) and 600 μM

ATP in buffer containing 30 mM Na Hepes pH 7.5, 100 mM NaCl, 0.2 mM $CaCl_2$, 10 mM $MgCl_2$, 2 mM DTT. Reactions were terminated following 5 min incubation with 5 nM CaMKII using ADP-Glo reagent (5 μL kinase reaction into mixture of 5 μL $H_2O$ and 10 μL ADP-Glo). After one hour, 20 μL detection reagent (Promega) was added before measurement of luminescence using a FLUOstar microplate reader (BMG Labtech).

**Isothermal titration calorimetry**. All ITC measurements were collected with a MicroCal PEAQTM (Malvern Panalyticial). Interactions with CaMKIIα peptides were performed at 25 °C in 25 mM HEPES pH 7.5 and 150 mM NaCl, with injections from a syringe containing 500 μM peptide into a cell containing 50 μM EF3-4. For interactions between Trx-CaMKIIα 1–315 variants and EF3-4, 2 mM $MgCl_2$ and 1 mM ADP were added to the buffer, and in this case the syringe was filled with 300 μM EF3-4 while the cell contained 30 μM Trx-CaMKIIα 1–315. In all cases, data was collected with 2 μL injections at 2 min intervals and constant mixing at 750 rpm. Bicinchoninic acid assays and A280 absorbance were used in tandem to determine protein concentrations. The same EF3-4 preparations were used for the ITC measurements presented in this study and previous measurements with WT CaMKII (Curtis et al., 2023). ITC data was collected and processed using MicroCal Origin software (Malvern Panalytical), using non-linear least-squares fitting to single binding models to estimate thermodynamic parameters.

**Hippocampal neuron culture and chemical LTP**

Dissociated hippocampal neurons were plated on 13 mm glass coverslips that had been pre-treated with poly-L-lysine (1 mg/mL) at $1\times10^5$ cells per coverslip. Neuronal cultures were maintained in neurobasal medium supplemented with B27, GlutaMAX, and Penicillin/Streptomycin. Neurons were transfected on DIV10 using 0.8 μg DNA and 2 μL

Lipofectamine-2000 per coverslip. N-FLAG-α-actinin-2 and N-V5-CaMKIIα variants were both expressed using pIRES2-GFP vectors. The AA variant was generated using site-directed mutagenesis with primers T305A&T306A_F and R (**supplemental Table S4**). For double transfections, 0.4 µg of each vector was included in the mixture. Cultures were maintained until chem-LTP and fixing on DIV14. Chem-LTP was induced by activating NMDARs with glycine (Fortin et al., 2010; McLeod et al., 2018). Neurons were first transferred into control solution (5 mM HEPES pH 7.4, 125 mM NaCl, 2.5 mM KCl, 1 mM $MgCl_2$, 2 mM $CaCl_2$, 33 mM D-glucose, 20 µM D-AP5, 3 µM strychnine, 20 µM bicuculline, 0.5 µM TTX) for 20 min at room temperature before cLTP was induced by 10-min incubation in cLTP solution (5 mM HEPES pH 7.4, 125 mM NaCl, 2.5 mM KCl, 2 mM $CaCl_2$, 33 mM D-glucose, 3 µM strychnine, 20 µM bicuculline, 0.2 mM glycine). Subsequently, neurons were returned to control solution to allow structural changes to develop before fixing in PBS supplemented with 4% paraformaldehyde, 4% sucrose, and 0.2% glutaraldehyde. Neurons were fixed two hours after induction of cLTP for PLA imaging, and four hours after cLTP induction for spine width analysis. Experiments involving rats were performed in accordance with the United Kingdom Animals Act, 1986 and within University College London Animal Research guidelines overseen by the UCL Animal Welfare and Ethical Review Body under project code 14058.

**Confocal imaging and PLA**

For spine width analysis, fixed neurons on glass coverslips were permeabilised for 5 min at RT in PBS supplemented with 1 % BSA/0.1 % Triton X-100, blocked for 1 hour in PBS supplemented with 10 % BSA and incubated overnight at 4 °C in 1 % BSA-PBS containing chicken anti-GFP (RRID_Ab: 300798, 1:500 dilution). On the following morning, neurons were washed and incubated for a further hour in 1 % BSA-PBS containing rabbit anti-chicken Alexa Fluor 488 (RRID_Ab:2339327. 1:500 dilution). After washing in PBS, coverslips were mounted on glass slides with ProLong Gold antifade mountant (Thermo Fisher) and sealed using nail varnish. PLAs were performed using reagents from a Duolink In Situ PLA kit. For PLAs, fixed neurons were permeabilised and blocked in the same way prior to overnight incubation with 1 % BSA containing the following primary antibodies: mouse anti-V5 (RRID_Ab: 10977225, 1:500 dilution); goat anti-FLAG (RRID_Ab: 10000565, 1:500 dilution); and chicken anti-GFP (1:500 dilution). On the following morning, neurons were washed then incubated with Duolink anti-mouse MINUS (DUO 92004) and anti-goat PLUS (DUO92003) probes along with rabbit anti-chicken Alexa Fluor 488 (1:500 dilution) for 1 hour at 37 °C. Probes were ligated at 37 °C for 30 min and signals were amplified at 37 °C for 100 min prior to mounting in ProLong Gold and sealing. Coverslips were imaged within 3 days of PLA labelling. In all cases, imaging was performed using a Zeiss LSM 780 microscope equipped with an airyscan module and using a 60× oil objective lens (Numerical Aperture = 1.40). Z-stacks of 0.38 μm optical slices were collected at 1024 × 1024 resolution. Images were collected using 488 nm excitation/521 nm emission for detecting anti-GFP labelling, and 594 nm excitation/619 nm emission for detecting PLA puncta. Images were analysed using NeuronStudio software (Icahn School of Medicine at Mount Sinai) to determine spine width and morphology; and the Distance Analysis (DiAna) plugin (Gilles et al., 2017) for ImageJ (NIH) to identify PLA puncta. For each neuron, spine or PLA puncta frequency per 10 μm dendrite was calculated across all clearly-resolved segments of the dendritic arbor.

**Measurement of miniature EPSCs**

mEPSCs were recorded 3-4 days after transfection from GFP-expressing primary hippocampal neurons transfected with either pIRES-CaMKIIα WT or AA. Control (GFP negative) neurons were recorded from the same coverslips. Neurons were visualized using an upright microscope (BX51WI; Olympus) equipped with a 20x NA objective (Olympus), fluorescence LED illumination (CoolLED pE-100), and filters (Chroma Technology ET470/40x, 495LP and ET 525/50m) for GFP visualization. The extracellular solution, adjusted to pH 7.3 with NaOH, contained: 145 mM NaCl, 2.5 mM KCl, 2 mM $CaCl_2$, 1 mM $MgCl_2$, 10 mM glucose, and 10 mM HEPES. To this we added 1 µM TTX, 20 µM D-AP5, and 20 µM SR-95531 to block voltage-gated sodium channels, NMDA receptors, and $GABA_A$ receptors, respectively. Whole-cell patch-clamp recordings were made using electrodes pulled from borosilicate glass that had a resistance of 5–7 MΩ when filled with an internal solution containing 140 mM CsCl, 2 mM NaCl, 2 mM $MgCl_2$, 0.5 mM $CaCl_2$, 2 mM $Na_2ATP$, 5 mM EGTA, 0.5 mM $Na_2GTP$, 2 mM QX-314 bromide and 10 mM HEPES (adjusted to pH 7.3 with CsOH). Recordings were made from four independent cultures after transfection using calcium phosphate. Currents were recorded at room temperature (22–26 °C) from cells voltage-clamped at −60 mV using an Axopatch 200B amplifier (Molecular Devices). Records were low-pass filtered at 2 kHz and sampled at 20 kHz using a Digidata 1200 interface and pClamp software (Molecular Devices). Series resistance ($R_{series}$) and input capacitance were read directly from the amplifier settings used to minimize the current responses to 5 mV hyperpolarizing voltage steps. $R_{series}$ (6.5–25.0 MΩ) was compensated (40–70 %) and monitored throughout each recording; if a cell showed a >30 % change in $R_{series}$ it was excluded from the analysis. The compensated $R_{series}$ was similar across the three experimental groups (4.9 ± 0.3, 4.8 ± 0.3 and 5.0 ± 0.5 MΩ, for control, WT and AA, respectively). All experiments were performed in an interleaved and blinded manner with unblinding only after completion of the analyses.

mEPSCs were detected using open-source Python software miniML, a deep learning-based detection method trained on a dataset of annotated mEPSCs from cerebellar mossy fiber to granule cell synapses (O'Neill et al., 2024). The pretrained cerebellar model was used directly, with a threshold of 0.6 applied to the prediction trace to extract data segments containing mEPSCs. Extracted events were examined individually using NeuroMatic running in Igor Pro (Wavemetrics) and the peak amplitudes and 10-90 % risetimes of single mEPSCs measured (Rothman and Silver, 2018). Spurious events were rejected. Overlapping currents and those with clearly notched rising phases, judged to result from closely-timed release events, were included in the calculation of mEPSC frequency but not amplitude. For each recording, an estimate of the baseline current noise was obtained by generating all-point amplitude histograms from 3–5 sections of the record, fitting the most negative current values in each with a single-sided Gaussian and averaging the obtained measures of standard deviation (range 2.3–6.3 pA), which did not differ across groups. The collected measures of individual mEPSC amplitude and 10-90 % risetime were analysed using R (version 4.3.1, the R Foundation for Statistical Computing) and RStudio (version 2024.04.2+764, Posit Software). Measures from untransfected cells from both groups were pooled and compared with those from the two groups of transfected cells. The mEPSC frequency was determined as the total number of mEPSCs detected/record length, and a mean mEPSC waveform was constructed from those events that displayed a monotonic rise and an uncontaminated decay.

### Experimental Design and Statistical Analyses

Each hippocampal culture was a mixed population derived from single litters of ~5 E18 Sprague Dawley pups of either sex. Imaging was performed using neurons derived from three independent cultures for PLA experiments and spine imaging. Miniature EPSCs were recorded from neurons deriving from two cultures, as described above. Normality of PLA and spine width data was confirmed using Kolmogorov-Smirnov testing prior to unpaired two-tailed Student's t-tests.

## Data availability

Coordinates and structure factors for crystal structures have been deposited with the RCSB Protein Databank with the following accession IDs: 7B55 (EF3-4 complex with apo CaMKIIα 1-

315); 7B56 (EF3-4 complex with CaMKIIα 1-315 + AMP-PNP); 7B57 (EF3-4 complex with CaMKIIα 1-315 + ADP).

## Results

### Interactions between CaMKIIα T305A/T306A and α-actinin-2 are elevated compared to those of WT CaMKIIα in unstimulated neurons

We first aimed to determine whether association of CaMKIIα AA and α-actinin-2 is elevated *in situ* relative to wild-type (WT) kinase using proximity ligation assays (PLA). We have previously shown that PLA can be used to monitor interactions between CaMKII and actinin in primary hippocampal neurons, and that chemical LTP (chem-LTP) triggers a marked increase in association of the two proteins (Curtis et al., 2023). Chem-LTP is considered a relatively realistic model of LTP (Lu et al., 2001; Fortin et al., 2010), in which cultured neurons are initially transferred for 20 min into a control solution containing pharmacological blockers that prevent spontaneous activity before 10 min incubation in a buffer containing glycine to activate NMDARs (Lu et al., 2001; Fortin et al., 2010). Rat primary hippocampal neurons were transfected on the tenth day *in vitro* (DIV10) with pIRES2-EGFP constructs for expression of FLAG-α-actinin-2 and V5-CaMKIIα variants to enable detection of actinin-CaMKII interactions by anti-FLAG/anti-V5 PLA after fixing on DIV14. Expression of either FLAG-α-actinin-2, V5-CaMKIIα WT or V5-CaMKIIα AA in isolation (**supplemental Fig. S1**) led to baseline levels of PLA puncta formation as expected. For neurons co-expressing FLAG-α-actinin-2 with V5-CaMKIIα WT, we detected 0.41 ± 0.05 PLA puncta per 10 μm dendrite (**Fig. 1b**, upper row). For this WT pairing, puncta frequency rose to 1.27 ± 0.06 per 10 μm ($P < 0.0001$) following chem-LTP (**Fig. 1b**, lower row) These values are in line with our previous work (Curtis et al., 2023). PLA puncta formation in naïve neurons co-expressing FLAG-α-actinin-2 and V5-CaMKIIα AA (**Fig. 1c**, upper row) was strikingly elevated at 1.14 ± 0.05 puncta per 10 μm – 2.8-fold higher than the equivalent condition with WT CaMKII ($P < 0.0001$). However, for the AA pairing, chem-LTP did not elevate puncta formation relative to naïve neurons (1.21 ±

0.04 puncta per 10 μm, **Fig. 1c**, lower row). PLA puncta frequencies are summarized in **Figure 1d**. Overall, our PLA imaging shows that interaction between CaMKIIα AA and α-actinin-2 is elevated in unstimulated neurons to a level only observed for WT kinase following the induction of LTP.

**The T305A/T306A CaMKIIα substitution increases spine size without altering synaptic currents**

Interactions between CaMKIIα and α-actinin-2 increase following chem-LTP, and disruption of these interactions prevents formation of large 'mushroom-type' dendritic spines (Hodges et al., 2014; Curtis et al., 2023; Saneyoshi, 2023). Given that the AA variant of CaMKIIα associates with α-actinin-2 in the absence of NMDAR activation (**Fig. 1c**, upper row), we hypothesised that spine morphology might be altered in naïve neurons expressing CaMKIIα AA. We determined the abundance of stubby (red), thin (amber), and mature mushroom-type (green) spines in primary hippocampal neurons expressing either FLAG-α-actinin-2 alone (**Fig. 2a**, leftmost column), WT or AA V5-CaMKIIα variants alone (second-from-left and middle columns), or each CaMKIIα variant in combination with FLAG-α-actinin-2 (right-most two columns). We compared spine types in both naïve neurons (**Fig. 2a**, upper row) and in neurons after induction of chem-LTP (lower row). We found that the abundance of particular spine types was influenced by expression of CaMKIIα AA (**Fig. 2a, b**). Mushroom-type spines were in a minority in naïve neurons that expressed only WT CaMKIIα. Neurons expressing FLAG-α-actinin alone projected $0.58 \pm 0.09$ mushroom spines per 10 μm dendritic length; those expressing V5-CaMKIIα WT alone or in combination with actinin presented $0.55 \pm 0.10$ and $0.69 \pm 0.06$, respectively. Expression of V5-CaMKIIα AA alone triggered a 4-fold increase in mushroom spine abundance to $2.17 \pm 0.18$ per 10 μm ($P < 0.001$) compared to neurons expressing only V5-CaMKIIα WT. A similar effect was seen in neurons co-expressing V5-CaMKIIα AA and α-actinin-2, with mushroom spine abundance rising to $2.09 \pm 0.19$ per 10 μm ($P < 0.001$) relative to the equivalent WT condition (**Fig. 2b**, upper row). Total spine densities were not statistically different between any of the five conditions before or after chem-LTP at approximately 3.5 spines per 10 μm for all conditions (**Fig. 2c**).

LTP is accompanied by an increase in spine width and proportion of spines with a mushroom-like structure, and this was evident in neurons expressing only WT CaMKIIα following chem-LTP with both mushroom spine abundance (**Fig. 2b**, lower row) and average spine width (**Fig. 2d**) increasing as expected. After chem-LTP, mushroom spines had become predominant in neurons expressing FLAG-α-actinin-2 alone (2.76 ± 0.20 per 10 μm, **Fig. 2b**, lower row), V5-CaMKIIα WT alone (2.20 ± 0.14), or V5-CaMKIIα WT in combination with α-actinin-2 (2.48 ± 0.17). Average spine width also increased for all three conditions: from 0.32 ± 0.01 to 0.57 ± 0.02 μm (α-actinin-2 only, $P < 0.001$), 0.33 ± 0.01 to 0.56 ± 0.01 (WT CaMKIIα only, $P < 0.001$), and 0.33 ± 0.01 to 0.56 ± 0.01 (WT CaMKIIα plus α-actinin-2, $P < 0.001$). However, spine morphology was little changed in neurons expressing CaMKIIα AA: neither spine type (**Fig. 2b**, lower row) nor spine width (**Fig. 2d**) was noticeably altered, with both characteristics now in line with the other experimental conditions. In sum, the spine imaging data indicates that the CaMKIIα AA substitution brings about morphological changes in unstimulated dendritic spines resembling those that occur in neurons expressing WT kinase following LTP.

In wild-type neurons, the size of dendritic spine heads typically scales with the amplitude of miniature excitatory postsynaptic currents (mEPSCs) (Matsuzaki et al., 2001; Noguchi et al., 2011). However, dissociation of these two attributes has been observed previously in neurons expressing mutated variants of CaMKIIα. For example, hippocampal primary neurons transfected with CaMKIIα T286D were found to develop larger spines but exhibited smaller EPSCs compared to WT controls (Pi et al., 2010b). To determine whether the changes in spine architecture brought about by CaMKIIα AA were accompanied by changes in synaptic currents, we recorded mEPSCs from untransfected neurons and neurons expressing either the WT or AA variant of CaMKIIα (**Fig. 3**). We isolated AMPAR-mediated mEPSCs by supplementing the extracellular solution with 1 μM

TTX, 20 µM D-AP5, and 20 µM SR-95531 to block voltage-gated sodium channels, NMDA receptors, and $GABA_A$ receptors, respectively. There was no difference in mEPSC mean amplitudes for the three groups: in untransfected neurons the mean amplitude was −22.0 ± 1.6 pA, (grey, **Fig. 3a, b**) compared to −20.2 ± 1.6 pA for neurons transfected with WT CaMKIIα (orange), and −21.7 ± 1.6 pA for the AA variant (green, $P$ = 0.93). mEPSC frequencies were variable but again no differences were detected between the three groups (**Fig. 3c** and **supplemental Table S1**). The same results were obtained when frequency and amplitude analysis was restricted to those (presumed proximal) mEPSCs having 10-90% risetimes of less than 1 ms (**supplemental Table S1**). Taken together, our data show that the CaMKIIα AA variant triggers increases in spine width and the proportion of mushroom-type spines without altering the mean amplitude of mEPSCs.

**Calorimetry with purified proteins confirms that the T305A/T306A CaMKIIα variant binds tightly to α-actinin-2**

Conventionally, effects of the AA substitution are attributed to decreases in phosphorylation at T305 and T306. In this case, one might attribute the increased association between α-actinin-2 and CaMKIIα brought about by the AA substitution to a decrease in phosphorylation at position T306 that occludes α-actinin-2 binding *in vitro* (Jalan-Sakrikar et al., 2012). However, *in vitro* binding studies show that interactions between CaMKIIα and α-actinin-2 are not affected by phosphorylation at T305 (Jalan-Sakrikar et al., 2012), consistent with a crystal structure showing the interface between the two proteins (Curtis et al., 2023). Therefore, one would expect any change in CaMKIIα – α-actinin-2 interaction resulting from suppression of inhibitory phosphorylation to be expressed in full by the single substitution T306A. However, single T306A substitution has no effect on *in situ* interactions between the two proteins (Curtis et al., 2023). An alternative explanation is that the AA variant has an unexpected gain-of-function ability to bind tightly to α-actinin-2 irrespective of any differences in phosphorylation. To rigorously investigate this possibility, we performed isothermal titration calorimetry (ITC) with purified proteins. α-actinin-2 EF hands 3-4 (EF3-4, orange, **Fig. 1a**) are the principal site for interactions with CaMKIIα (Jalan-Sakrikar et al., 2012; Curtis et al., 2023). We previously showed that EF3-4 binds isolated WT CaMKIIα regulatory segment (294-315) with $K_d$ = 32 ± 1 μM, whereas interactions between EF3-4 and a CaMKIIα construct that includes both the kinase domain and regulatory segment (1-315) are so weak as to be undetectable by ITC. Here, we performed equivalent measurements using CaMKIIα 1-315 (**Fig. 4a-c**) constructs or regulatory segment peptides (**Fig. 4d-f)** bearing single or double alanine substitutions at T305 and T306. Measurements with single alanine substitutions yielded similar results to the WT sequence. It was not possible to detect interactions between EF3-4 and CaMKIIα T305A or T306A in the context of the longer 1-315 construct (**Fig. 4a, b**). Furthermore, EF3-4 bound to T305A regulatory segment peptide with $K_d$ = 19.4 ± 0.7 μM (**Fig. 4d**), and to the T306A equivalent with $K_d$ = 19.8 ± 1.9 μM (**Fig. 4e**), recapitulating the result with WT construct (Curtis et al., 2023). Remarkably, CaMKIIα (1-315) AA bound tightly to EF3-4 with $K_d$ = 154 ± 9 nM (**Fig. 4c**), which is 100-fold tighter than even the interaction between EF3-4 and isolated WT regulatory segment. Surprisingly, though, the AA substitution did not markedly alter interactions in the context of the isolated regulatory segment with interaction to EF3-4 occurring with $K_d$ = 14.7 ± 1.2 μM in this case (**Fig. 4f**). This suggests that high affinity interactions between the AA variant and α-actinin-2 involve CaMKIIα elements beyond positions 294-315. Full thermodynamic parameters obtained for all ITC measurements are shown in **supplemental Table S2**.

Previous studies have indicated that the AA substitution may also somewhat increase CaMKII sensitivity to CaM (Chang et al., 2017). We compared the rate of CaMKII phosphorylation of syntide-2 with different concentrations of CaM for purified WT (**Fig. 4g**) and AA CaMKIIα (**Fig. 4h**). The AA variant responded to CaM at lower concentrations ($EC_{50}$ = 44 ± 3 nM, Hill coefficient = 2.6 ± 0.3) than WT ($EC_{50}$ = 195 ± 20 nM, Hill coefficient = 1.6. ± 0.2). Neither CaMKII variant exhibited any activation with 1 μM EF3-4 (right-hand sub-panels, **Fig. 4g, h**), which is also consistent with previous work (Jalan-Sakrikar et al., 2012). Overall, our kinase assay and ITC data reveal that while the AA substitution slightly increases sensitivity to $Ca^{2+}$/CaM, it enables α-actinin-2 to bind tightly to inactive CaMKIIα, with alanine substitutions at both T305 and T306 necessary to bring about this effect.

**Molecular basis of high affinity association between α-actinin-2 and the T305A/T306A variant** CaMKIIα (1-315) AA bound to EF3-4 tightly, whereas a peptide spanning residues 294-315 of CaMKIIα AA did not. This indicates that the AA variant binds α-actinin-2 using an unanticipated binding mode. To understand the molecular basis of the interaction, we determined crystal structures of a complex between EF3-4 and CaMKIIα (1-315) AA (**Fig. 5a**). Structures were determined with either no nucleotide (PDB ID 7B55; 1.6 Å resolution, **supplemental Fig. S2a**), with $Mg^{2+}$/AMP-PNP (PDB ID 7B56; 1.45 Å resolution, **supplemental Fig. S2b**), or with $Mg^{2+}$/ADP (PDB ID 7B57; 1.95 Å resolution, **supplemental Fig. S2c**). Full crystallographic statistics are shown in **supplemental Table S3**. In the nucleotide-free complex, a MES molecule occupies the nucleotide-binding site (**supplemental Fig. S2a**). The three structures are broadly similar (**supplemental Fig. S2d**), with RMSD for all Cα positions of 0.63 Å (7B55-7B56), 0.53 Å (7B55-7B57), and 0.371 Å (7B56-7B57). The structures are most different in the vicinity of the nucleotide-binding pocket (**supplemental Fig. S2e-g**), but α-actinin-2 and CaMKIIα AA interact in the same way in all three cases. Our analysis focuses on the complex with ADP (7B57). In the complex, CaMKIIα kinase domain (green, **Fig. 5b**) adopts a similar conformation to that observed in other structures of auto-inhibited CaMKIIα (Chao et al., 2011). For example, alignment of CaMKIIα positions 7-300 between the $Mg^{2+}$/ADP complex structure solved here and the equivalent region in a full-length autoinhibited CaMKIIα construct (3SOA) (Chao et al., 2011) gives RMSD of 0.79 Å. Electron density is visible for the CaMKIIα regulatory segment up to residue M307, with the regulatory segment exiting the kinase domain in the vicinity of the glycine rich nucleotide-coordinating loop (**Fig. 5b**). The α-actinin-2 EF3-4 region (orange, **Fig. 5b**) forms an extensive interface with the CaMKIIα regulatory segment (blue), which presents a series of aliphatic sidechains on the side opposite to the kinase domain including A295, L299, A302, and I303 (**Fig. 5c, d**). Van der Waals interactions between these amino acids and EF3-4 residues F835, V831, L854, and C862 make up the core of the interface (**Fig. 5c, d**). A further hydrophobic interaction occurs between the sidechains of $M307_{CaMKII}$ and $Y861_{EF3\text{-}4}$ (**Fig. 5d**). The interface is supported by hydrogen bonds at either end: the amine group of $K292_{CaMKII}$ H-bonds with the main-chain oxygen of $I837_{EF3\text{-}4}$ (**Fig. 5c**); and the main-chain oxygen of $A302_{CaMKII}$ H-bonds with the hydroxyl group of $Y889_{EF3\text{-}4}$ (**Fig. 5c, d**). Finally, the interface includes a salt-bridge between the sidechains of $R296_{CaMKII}$ and $E853_{EF3\text{-}4}$ (**Fig. 5d**).

Comparison to structures of WT CaMKIIα regulatory segments in complex with α-actinin-2 and CaM reveals that the AA substitution supports a binding mode that has not been observed before. **Fig. 6** shows aligned structures of WT CaMKII regulatory segment in complex with $Ca^{2+}$/CaM (PDB 2WEL, **Fig. 6a**) (Rellos et al., 2010) and α-actinin-2 EF3-4 (PDB 6TS3, **Fig. 6b**) (Curtis et al., 2023) alongside the structure of AA-variant regulatory segment in complex with EF3-4 (**Fig. 6c**) extracted from the $Mg^{2+}$/ADP structure solved in this study (PDB 7B57). The CaM complex involves the δ isoform of CaMKII (**Fig. 6b**) but this isoform is identical in the regulatory region corresponding to positions 282-315 in CaMKIIα. Equivalent side-on views of the CaMKII regulatory segment are shown in **Fig. 6a-c**, with each structure centred on T305. A perpendicular view along the axis of the regulatory segment α-helix is also shown in each case (**Fig. 6a-c**, right-hand sub-panels). $Ca^{2+}$/CaM fully envelopes the CaMKII regulatory segment (**Fig. 6a**), which explains why CaM binds much more tightly to isolated regulatory segment or pT286-activated CaMKII where steric hindrance by the kinase domain is absent or reduced (Putkey and Waxham, 1996; Waxham et al., 1998). EF3-4 binds predominantly to the C-terminal part of WT CaMKIIα regulatory segment (**Fig. 6b**), with direct interactions to CaMKII spanning positions L299 to F313. EF3-4 is rotated by ~50° relative to the third and fourth EF hands of CaM around the axis of the regulatory segment helix, with the third EF hand positioned in the foreground according to the view in **Fig. 6** (right-hand column) in both cases. Structural alignment of isolated CaMKII regulatory segments or EF3-4 domains from the WT and AA complexes shows that each separate polypeptide retains a highly similar conformation in both complexes (**Fig. 6d, e**). However, the relative orientation of the two binding elements is markedly altered (**Fig. 6b, c**). In the complex with CaMKIIα (1-315) AA, EF3-4 binding is shifted towards the N-terminus of the regulatory segment (**Fig. 6c**) with direct interactions extending up to CaMKII position K291 and only reaching M307 in the C-terminal direction. Most strikingly, EF3-4 is flipped according to the view in **Fig. 6a-c** (right-hand column) with the fourth EF hand (light orange) in the foreground unlike the other two complexes.

The much higher affinity of EF3-4 for CaMKIIα AA residues 1-315 compared to 294-315 (**Figs. 4c, f**) led us to suspect that EF3-4 contacts elements within the kinase domain of the AA variant. However, the structure reveals no direct interactions involving the kinase domain (**Fig. 7a**). Instead, substitution of alanine at positions 305 and 306 enables EF3-4 to invert its third and fourth EF hands and mediate a different network of interactions to the regulatory segment with a shift of approximately two helical turns towards the N-terminus of the segment. In this new binding mode, A306 mediates van der Waals interactions with L888$_{EF3\text{-}4}$ and F884 $_{EF3\text{-}4}$ and the substitution at position 305 provides access for a H-bond between the hydroxyl group of Y889$_{EF3\text{-}4}$ and the main-chain carbonyl of A302$_{CaMKII}$ (**Fig. 7b**). At the N-terminal end of the segment, the side-chain of K291$_{CaMKII}$ packs against I837$_{EF3\text{-}4}$ (**Fig. 7c**). In addition, the terminal amine of K292$_{CaMKII}$ H-bonds with the main-chain oxygen of I837$_{EF3\text{-}4}$ and also forms a water-mediated H-bond with the side-chain of E853$_{EF3\text{-}4}$. To confirm that the higher affinity of α-actinin-2 for the AA CaMKIIα variant results from these additional interactions, we performed further ITC measurements with N-terminally shifted regulatory segment peptides starting at position 290 (**Fig. 7d, e**). The peptides were limited to 20-mers extending to position 309 – the minimal region sufficient for binding according to the mode observed in the crystal structure (**Fig. 4**). Consistent with the binding mode in the crystals, EF3-4 bound to AA CaMKIIα 290-309 more than 20-fold more tightly ($K_d$ = 146 ± 12 nM, **Fig. 7e**) than to the WT equivalent (3.46 ± 0.08 μM, **Fig. 7d**) with a dissociation constant comparable to the 1-315 construct (**Fig. 4c**, Kd = 154 ± 9 nM). In sum, our structural and ITC data show that the AA substitution allows α-actinin-2 to adopt a different higher-affinity binding mode that involves extensive interactions with N-terminal elements of the CaMKII regulatory segment.

## Discussion

In this study, we show that the AA substitution in CaMKII$\alpha$ gives rise to the gain-of-function ability to bind $\alpha$-actinin-2 tightly (**Fig. 1c**); calorimetry reveals a binding affinity of ~150 nM (**Fig. 4c**). EF3-4 adopts a different binding mode when associating with the AA variant, and – unlike the WT sequence (Curtis et al., 2023) – its interface on CaMKII$\alpha$ is fully accessible when the kinase is inactive (**Fig. 5**). Expression of the AA variant in cultured neurons increases the proportion of mushroom-type dendritic spines in unstimulated neurons (**Fig. 2b**). Previous studies have shown that $\alpha$-actinin-2 is essential for the development of enlarged mushroom-type spines during LTP through interactions with CaMKII$\alpha$ (Hodges et al., 2014; Curtis et al., 2023). Our findings suggest that the AA variant provides a shortcut to this structural component of LTP by interacting tightly with $\alpha$-actinin-2 with no requirement for LTP induction to potentiate the interaction (Curtis et al., 2023; Saneyoshi, 2023).

Our findings are consistent with a study that employed the CaMKII$\alpha$ AA variant for purified $\alpha$-actinin-2 pull-downs and found these to be more robust than for the WT kinase (Jalan-Sakrikar et al., 2012). Prior work indicates that phosphorylation of T306 but not T305 could potentially inhibit interactions between CaMKII and $\alpha$-actinin-2 (Jalan-Sakrikar et al., 2012). T305 projects away from the interface between WT CaMKII and $\alpha$-actinin-2 (Curtis et al., 2023). Prolonged *in vitro* incubation of autonomously-active T305A (but not T306A) CaMKII reduces $\alpha$-actinin-2 pull-down with CaMKII$\alpha$ (Jalan-Sakrikar et al., 2012). On this basis, one would expect any increase in CaMKII-actinin association deriving from suppression of inhibitory phosphorylation to be expressed in full by the T305A variant. However, we found previously that T305A CaMKII$\alpha$

behaved like WT kinase, with α-actinin-2 interactions increasing markedly after chem-LTP (Curtis et al., 2023). We have also analysed spine morphology in images collected previously of hippocampal neurons expressing either T305A or T306A CaMKIIα (Curtis et al., 2023). These single-mutation variants exhibit spine morphologies like WT CaMKIIα, with spine head diameter and the proportion of mushroom-type spines increasing following chem-LTP (**supplemental Fig. S3**). This reinforces the notion that the effects of the AA substitution on interactions with actinin are an intrinsic property of the protein sequence rather than an indirect effect due to blocking of inhibitory phosphorylation. Unanticipated effects of alanine substitutions have been documented previously. For example, the active site mutant C146A form of Ubp8 unexpectedly binds tightly to, and sequesters, ubiquitin (Morrow et al., 2018). Synergistic effects of multiple alanine substitutions have been observed in a screen of alanine-substituted peptide binders to the oncogenic protein MDM2 (Ye et al., 2022), and alanine substitutions at three positions in an inhibitor peptide derived from CaMKIIN also unexpectedly increased potency (Coultrap and Bayer, 2011).

The gain-of-function ability to bind tightly to α-actinin-2 provides an alternative explanation for the effects of the AA substitution in CaMKIIα but does not rule out the possibility that phosphorylation at T305 and/or T306 is important. What then is the evidence that these sites are phosphorylated? CaMKII preferentially phosphorylates serine/threonine residues when arginine is present 3 residues upstream (the '-3' position): mutation of the -3 arginine in a model substrate peptide led to a ~300-fold decrease in catalytic efficiency including an ~80-fold decrease in $V_{max}$ (White et al., 1998). Furthermore, the presence of a non-hydrophobic residue at the -5 position greatly decreases phosphorylation (White et al., 1998). According to these criteria, one would expect T286 to be a good substrate (MHRQE**T**), T305 to be an extremely poor substrate (KGAIL**T**), and T306 to be a poor substrate (KGAILT**T**). A quantitative proteomic study performed with purified

CaMKIIα fits with what would be expected from the primary sequence: Baucum and co-workers measured phosphorylation at specific sites before and after $Ca^{2+}$/CaM stimulation, and also in a third phase dependent on autonomous activity. T286 was robustly phosphorylated in the second phase (~80 %), whereas T306 phosphorylation was elevated to ~10 % after the third phase (lower than many other sites) and T305 phosphorylation could not be detected (Baucum et al., 2015). For inhibitory phosphorylation at T305 or T306 to meaningfully inhibit subsequent $Ca^{2+}$/CaM activation, one would expect that it would occur at higher levels than observed in this study under idealised circumstances. An alternative role for T305/T306 phosphorylation is targeting to inhibitory synapses (Cook et al., 2021) – this mechanism is more compatible with inefficient T305/T306 phosphorylation, e.g., pT306 in a single CaMKII protomer could be sufficient for targeting a full dodecamer. In general, it is difficult to reliably monitor phosphorylation at specific sites in cells. Experiments with phospho-specific antibodies do not reveal proportional levels of phosphorylation. Mass spectrometry (MS)-based quantitation of absolute protein abundance was key to building realistic models of the postsynaptic density (Cheng et al., 2006; Gold, 2012). It is much more challenging to apply proteomics to quantify phosphorylation levels at specific amino acids, but studies of this type (Bruning et al., 2019) would help to distinguish which specific sites are important during synaptic plasticity.

The AA substitution is frequently combined with the phospho-mimetic change T286D – this 'D/AA' variant is considered a 'constitutively-active' form of CaMKII that increases both dendritic spine size and AMPAR current amplitudes with no need for a $Ca^{2+}$ impulse (Pi et al., 2010b; Pi et al., 2010a; Barcomb et al., 2014; Chang et al., 2017; Diaz-Alonso et al., 2017; Rossetti et al., 2017; Chang et al., 2019; Ye et al., 2019; Chen et al., 2024). While CaMKIIα D/AA increases AMPAR current amplitudes, expression of the T286D substitution alone has the opposite effect (Pi et al., 2010b). One interpretation of this result is that when threonine is present at positions 305 and

306, CaMKIIα auto-phosphorylates at these sites due to its autonomous activity, which prevents its full activation by $Ca^{2+}$/CaM (Pi et al., 2010b). However, this explanation doesn't account for the finding that the T286D substitution also depresses AMPAR currents when introduced in combination with the kinase-inactivating mutation K42R (Pi et al., 2010b). Experiments with Camui-α, which reports on the activation state of CaMKIIα, also cast doubt on the conventional interpretation (Chang et al., 2017). The basal fluorescent lifetime of Camui-α was found to be elevated in variants that included the T286D substitution either alone or in combination with the AA substitution (Chang et al., 2017). However, both forms showed a small but similar increase in activation upon glutamate uncaging indicating that the AA substitution does not noticeably alter the ability of $Ca^{2+}$/CaM to activate CaMKII bearing the T286D mutation. Our finding that the AA substitution binds tightly to α-actinin-2 provides a more congruent explanation for the strongly potentiating behaviour of the D/AA mutation. α-actinin-2 is enriched in dendritic spines, and it interacts with several core postsynaptic proteins including NMDARs (Wyszynski et al., 1997), PSD-95 (Matt et al., 2018), and densin-180 (Walikonis et al., 2001). Targeting autonomously-active CaMKII to this compartment may accurately mimic LTP, in which stable interactions between CaMKII and proteins including NMDARs and actinin are a key feature (Saneyoshi, 2023; Tullis et al., 2023). Furthermore, we found that CaMKIIα AA could be activated by somewhat lower concentrations of CaM (**Fig. 4h**), which probably contributes to its synaptic effects. The AA substitution may also alter interactions to other synaptic proteins including NMDARs either directly or via elevated actinin/CaM binding (Robison et al., 2005). Interestingly, we found that CaMKIIα AA expression did not alter the amplitude of mEPSCs in cultured hippocampal primary neurons (**Fig. 3d, e**). This suggests that the actinin-CaMKII interaction can mediate structural changes – likely via remodelling of the actin cytoskeleton (Saneyoshi, 2023) – without increasing AMPAR currents, and implies that interactions involving the CaMKII kinase domain are required for the full expression of LTP.

The importance of structural rather than enzymatic protein function is an emerging theme in the mechanics of synaptic plasticity (Yasuda et al., 2022; Tullis et al., 2023). Experiments with a different abundant PSD protein reinforce this theme: mutations within the GTPase-activating protein (GAP) domain of SynGAP do not inhibit synaptic plasticity (Araki et al., 2024). Instead, SynGAP is thought to modulate synaptic strength by physically competing with AMPAR-TARP complexes for recruitment to PSD-95 (Araki et al., 2024). The ability of CaMKII to render itself autonomously active via auto-phosphorylation was reasonably considered as a mechanism for long-term memory storage (Lisman et al., 2012). However, imaging with reporters of CaMKII conformation shows that kinase activity only lasts for a matter of seconds after NMDAR activation (Lee et al., 2009; Fujii et al., 2013). Consistent with these studies, CaMKII photo-inhibition has no effect on LTP if delayed until one minute after LTP induction (Murakoshi et al., 2017). The function of T286 phosphorylation is now thought to be limited to the initiation phase (Buard et al., 2010) including detecting specific $Ca^{2+}$ signal frequencies in LTP induction while playing no role in LTP maintenance (Chang et al., 2017). Our findings further downplay phosphorylation-based regulation of CaMKII activity and reinforce the concept that highly abundant synaptic enzymes can operate primarily through their ability to mediate protein-protein interactions.

## References


Anggono V, Huganir RL (2012) Regulation of AMPA receptor trafficking and synaptic plasticity. Curr Opin Neurobiol 22:461-469.

Araki Y, Rajkovich KE, Gerber EE, Gamache TR, Johnson RC, Tran THN, Liu B, Zhu Q, Hong I, Kirkwood A, Huganir R (2024) SynGAP regulates synaptic plasticity and cognition independently of its catalytic activity. Science 383:eadk1291.

Barcomb K, Buard I, Coultrap SJ, Kulbe JR, O'Leary H, Benke TA, Bayer KU (2014) Autonomous CaMKII requires further stimulation by Ca2+/calmodulin for enhancing synaptic strength. FASEB J 28:3810-3819.

Baucum AJ, 2nd, Shonesy BC, Rose KL, Colbran RJ (2015) Quantitative proteomics analysis of CaMKII phosphorylation and the CaMKII interactome in the mouse forebrain. ACS Chem Neurosci 6:615-631.

Bayer KU, De Koninck P, Leonard AS, Hell JW, Schulman H (2001) Interaction with the NMDA receptor locks CaMKII in an active conformation. Nature 411:801-805.

Bruning F, Noya SB, Bange T, Koutsouli S, Rudolph JD, Tyagarajan SK, Cox J, Mann M, Brown SA, Robles MS (2019) Sleep-wake cycles drive daily dynamics of synaptic phosphorylation. Science 366:aav3617.

Buard I, Coultrap SJ, Freund RK, Lee YS, Dell'Acqua ML, Silva AJ, Bayer KU (2010) CaMKII "autonomy" is required for initiating but not for maintaining neuronal long-term information storage. The Journal of neuroscience : the official journal of the Society for Neuroscience 30:8214-8220.

Chang JY, Nakahata Y, Hayano Y, Yasuda R (2019) Mechanisms of Ca(2+)/calmodulin-dependent kinase II activation in single dendritic spines. Nature communications 10:2784.

Chang JY, Parra-Bueno P, Laviv T, Szatmari EM, Lee SR, Yasuda R (2017) CaMKII Autophosphorylation Is Necessary for Optimal Integration of Ca(2+) Signals during LTP Induction, but Not Maintenance. Neuron 94:800-808 e804.

Chao LH, Stratton MM, Lee IH, Rosenberg OS, Levitz J, Mandell DJ, Kortemme T, Groves JT, Schulman H, Kuriyan J (2011) A mechanism for tunable autoinhibition in the structure of a human Ca2+/calmodulin- dependent kinase II holoenzyme. Cell 146:732-745.

Chen X, Cai Q, Zhou J, Pleasure SJ, Schulman H, Zhang M, Nicoll RA (2024) CaMKII autophosphorylation is the only enzymatic event required for synaptic memory. Proc Natl Acad Sci U S A 121:e2402783121.

Cheng D, Hoogenraad CC, Rush J, Ramm E, Schlager MA, Duong DM, Xu P, Wijayawardana SR, Hanfelt J, Nakagawa T, Sheng M, Peng J (2006) Relative and absolute quantification of postsynaptic density proteome isolated from rat forebrain and cerebellum. Mol Cell Proteomics 5:1158-1170.

Cook SG, Buonarati OR, Coultrap SJ, Bayer KU (2021) CaMKII holoenzyme mechanisms that govern the LTP versus LTD decision. Sci Adv 7:eabe2300.

Coultrap SJ, Bayer KU (2011) Improving a natural CaMKII inhibitor by random and rational design. PLoS One 6:e25245.

Curtis AJ, Zhu J, Penny CJ, Gold MG (2023) Molecular basis of interactions between CaMKII and alpha-actinin-2 that underlie dendritic spine enlargement. Elife 12:eLife.85008.

Diaz-Alonso J, Sun YJ, Granger AJ, Levy JM, Blankenship SM, Nicoll RA (2017) Subunit-specific role for the amino-terminal domain of AMPA receptors in synaptic targeting. Proc Natl Acad Sci U S A 114:7136-7141.

Erondu NE, Kennedy MB (1985) Regional distribution of type II Ca2+/calmodulin-dependent protein kinase in rat brain. The Journal of neuroscience : the official journal of the Society for Neuroscience 5:3270-3277.

Evans PR, Murshudov GN (2013) How good are my data and what is the resolution? Acta Crystallogr D Biol Crystallogr 69:1204-1214.

Fortin DA, Davare MA, Srivastava T, Brady JD, Nygaard S, Derkach VA, Soderling TR (2010) Long-term potentiation-dependent spine enlargement requires synaptic Ca2+-permeable AMPA receptors recruited by CaM-kinase I. The Journal of neuroscience : the official journal of the Society for Neuroscience 30:11565-11575.

Fujii H, Inoue M, Okuno H, Sano Y, Takemoto-Kimura S, Kitamura K, Kano M, Bito H (2013) Nonlinear decoding and asymmetric representation of neuronal input information by CaMKIIalpha and calcineurin. Cell Rep 3:978-987.

Gold MG (2012) A frontier in the understanding of synaptic plasticity: solving the structure of the postsynaptic density. Bioessays 34:599-608.

Hanson PI, Schulman H (1992) Inhibitory autophosphorylation of multifunctional Ca2+/calmodulin-dependent protein kinase analyzed by site-directed mutagenesis. J Biol Chem 267:17216-17224.

Hell JW (2014) CaMKII: claiming center stage in postsynaptic function and organization. Neuron 81:249-265.

Hodges JL, Vilchez SM, Asmussen H, Whitmore LA, Horwitz AR (2014) alpha-Actinin-2 mediates spine morphology and assembly of the post-synaptic density in hippocampal neurons. PLoS One 9:e101770.

Incontro S, Diaz-Alonso J, Iafrati J, Vieira M, Asensio CS, Sohal VS, Roche KW, Bender KJ, Nicoll RA (2018) The CaMKII/NMDA receptor complex controls hippocampal synaptic transmission by kinase-dependent and independent mechanisms. Nat Commun 9:2069.

Jalan-Sakrikar N, Bartlett RK, Baucum AJ, 2nd, Colbran RJ (2012) Substrate-selective and calcium-independent activation of CaMKII by alpha-actinin. J Biol Chem 287:15275-15283.

Krissinel E (2012) Enhanced fold recognition using efficient short fragment clustering. J Mol Biochem 1:76-85.

Lee SJ, Escobedo-Lozoya Y, Szatmari EM, Yasuda R (2009) Activation of CaMKII in single dendritic spines during long-term potentiation. Nature 458:299-304.

Liebschner D et al. (2019) Macromolecular structure determination using X-rays, neutrons and electrons: recent developments in Phenix. Acta Crystallogr D Struct Biol 75:861-877.

Lisman J, Yasuda R, Raghavachari S (2012) Mechanisms of CaMKII action in long-term potentiation. Nat Rev Neurosci 13:169-182.

Lu W, Man H, Ju W, Trimble WS, MacDonald JF, Wang YT (2001) Activation of synaptic NMDA receptors induces membrane insertion of new AMPA receptors and LTP in cultured hippocampal neurons. Neuron 29:243-254.

Matsuzaki M, Ellis-Davies GC, Nemoto T, Miyashita Y, Iino M, Kasai H (2001) Dendritic spine geometry is critical for AMPA receptor expression in hippocampal CA1 pyramidal neurons. Nat Neurosci 4:1086-1092.

Matt L, Kim K, Hergarden AC, Patriarchi T, Malik ZA, Park DK, Chowdhury D, Buonarati OR, Henderson PB, Gokcek Sarac C, Zhang Y, Mohapatra D, Horne MC, Ames JB, Hell JW (2018) alpha-Actinin Anchors PSD-95 at Postsynaptic Sites. Neuron 97:1094-1109 e1099.

McCoy AJ, Grosse-Kunstleve RW, Adams PD, Winn MD, Storoni LC, Read RJ (2007) Phaser crystallographic software. J Appl Crystallogr 40:658-674.

McLeod F, Bossio A, Marzo A, Ciani L, Sibilla S, Hannan S, Wilson GA, Palomer E, Smart TG, Gibb A, Salinas PC (2018) Wnt Signaling Mediates LTP-Dependent Spine Plasticity and AMPAR Localization through Frizzled-7 Receptors. Cell Rep 23:1060-1071.

Miller SG, Patton BL, Kennedy MB (1988) Sequences of autophosphorylation sites in neuronal type II CaM kinase that control Ca2(+)-independent activity. Neuron 1:593-604.

Morrow ME, Morgan MT, Clerici M, Growkova K, Yan M, Komander D, Sixma TK, Simicek M, Wolberger C (2018) Active site alanine mutations convert deubiquitinases into high-affinity ubiquitin-binding proteins. EMBO Rep 19:201745680.

Murakoshi H, Shin ME, Parra-Bueno P, Szatmari EM, Shibata ACE, Yasuda R (2017) Kinetics of Endogenous CaMKII Required for Synaptic Plasticity Revealed by Optogenetic Kinase Inhibitor. Neuron 94:690.

Myers JB, Zaegel V, Coultrap SJ, Miller AP, Bayer KU, Reichow SL (2017) The CaMKII holoenzyme structure in activation-competent conformations. Nature communications 8:15742.

Noguchi J, Nagaoka A, Watanabe S, Ellis-Davies GC, Kitamura K, Kano M, Matsuzaki M, Kasai H (2011) In vivo two-photon uncaging of glutamate revealing the structure-function relationships of dendritic spines in the neocortex of adult mice. J Physiol 589:2447-2457.

O'Neill PS, Baccino-Calace M, Rupprecht P, Friedrich RW, Delvendahl MM (2024) A deep learning framework for automated and generalized synaptic event analysis. eLife:98485.

Ozden C, Sloutsky R, Mitsugi T, Santos N, Agnello E, Gaubitz C, Foster J, Lapinskas E, Esposito EA, Saneyoshi T, Kelch BA, Garman SC, Hayashi Y, Stratton MM (2022) CaMKII binds both substrates and activators at the active site. Cell Rep 40:111064.

Penny CJ, Gold MG (2018) Mechanisms for localising calcineurin and CaMKII in dendritic spines. Cell Signal 49:46-58.

Pi HJ, Otmakhov N, Lemelin D, De Koninck P, Lisman J (2010a) Autonomous CaMKII can promote either long-term potentiation or long-term depression, depending on the state of T305/T306 phosphorylation. The Journal of neuroscience : the official journal of the Society for Neuroscience 30:8704-8709.

Pi HJ, Otmakhov N, El Gaamouch F, Lemelin D, De Koninck P, Lisman J (2010b) CaMKII control of spine size and synaptic strength: role of phosphorylation states and nonenzymatic action. Proc Natl Acad Sci U S A 107:14437-14442.

Putkey JA, Waxham MN (1996) A peptide model for calmodulin trapping by calcium/calmodulin-dependent protein kinase II. J Biol Chem 271:29619-29623.

Rellos P, Pike AC, Niesen FH, Salah E, Lee WH, von Delft F, Knapp S (2010) Structure of the CaMKIIdelta/calmodulin complex reveals the molecular mechanism of CaMKII kinase activation. PLoS Biol 8:e1000426.

Robison AJ, Bass MA, Jiao Y, MacMillan LB, Carmody LC, Bartlett RK, Colbran RJ (2005) Multivalent interactions of calcium/calmodulin-dependent protein kinase II with the postsynaptic density proteins NR2B, densin-180, and alpha-actinin-2. J Biol Chem 280:35329-35336.

Rossetti T, Banerjee S, Kim C, Leubner M, Lamar C, Gupta P, Lee B, Neve R, Lisman J (2017) Memory Erasure Experiments Indicate a Critical Role of CaMKII in Memory Storage. Neuron 96:207-216 e202.

Rothman JS, Silver RA (2018) NeuroMatic: An Integrated Open-Source Software Toolkit for Acquisition, Analysis and Simulation of Electrophysiological Data. Front Neuroinform 12:14.

Saneyoshi T (2023) Changing the size of dendritic spines. Elife 12:eLife.91566.

Schworer CM, Colbran RJ, Keefer JR, Soderling TR (1988) Ca2+/calmodulin-dependent protein kinase II. Identification of a regulatory autophosphorylation site adjacent to the inhibitory and calmodulin-binding domains. J Biol Chem 263:13486-13489.

Shen K, Teruel MN, Connor JH, Shenolikar S, Meyer T (2000) Molecular memory by reversible translocation of calcium/calmodulin-dependent protein kinase II. Nat Neurosci 3:881-886.

Takeuchi T, Duszkiewicz AJ, Morris RG (2014) The synaptic plasticity and memory hypothesis: encoding, storage and persistence. Philos Trans R Soc Lond B Biol Sci 369:20130288.

Thiel G, Czernik AJ, Gorelick F, Nairn AC, Greengard P (1988) Ca2+/calmodulin-dependent protein kinase II: identification of threonine-286 as the autophosphorylation site in the alpha subunit associated with the generation of Ca2+-independent activity. Proc Natl Acad Sci U S A 85:6337-6341.

Tullis JE, Larsen ME, Rumian NL, Freund RK, Boxer EE, Brown CN, Coultrap SJ, Schulman H, Aoto J, Dell'Acqua ML, Bayer KU (2023) LTP induction by structural rather than enzymatic functions of CaMKII. Nature 621:146-153.

Walikonis RS, Oguni A, Khorosheva EM, Jeng CJ, Asuncion FJ, Kennedy MB (2001) Densin-180 forms a ternary complex with the (alpha)-subunit of Ca2+/calmodulin-dependent protein kinase II and (alpha)-actinin. The Journal of neuroscience : the official journal of the Society for Neuroscience 21:423-433.

Waxham MN, Tsai AL, Putkey JA (1998) A mechanism for calmodulin (CaM) trapping by CaM-kinase II defined by a family of CaM-binding peptides. J Biol Chem 273:17579-17584.

White RR, Kwon YG, Taing M, Lawrence DS, Edelman AM (1998) Definition of optimal substrate recognition motifs of Ca2+-calmodulin-dependent protein kinases IV and II reveals shared and distinctive features. J Biol Chem 273:3166-3172.

Winter G, Waterman DG, Parkhurst JM, Brewster AS, Gildea RJ, Gerstel M, Fuentes-Montero L, Vollmar M, Michels-Clark T, Young ID, Sauter NK, Evans G (2018) DIALS: implementation and evaluation of a new integration package. Acta Crystallogr D Struct Biol 74:85-97.

Wyszynski M, Lin J, Rao A, Nigh E, Beggs AH, Craig AM, Sheng M (1997) Competitive binding of alpha-actinin and calmodulin to the NMDA receptor. Nature 385:439-442.

Yasuda R, Hayashi Y, Hell JW (2022) CaMKII: a central molecular organizer of synaptic plasticity, learning and memory. Nat Rev Neurosci 23:666-682.

Ye S, Kim JI, Kim J, Kaang BK (2019) Overexpression of activated CaMKII in the CA1 hippocampus impairs context discrimination, but not contextual conditioning. Mol Brain 12:Article number 32.

Ye X, Lee YC, Gates ZP, Ling Y, Mortensen JC, Yang FS, Lin YS, Pentelute BL (2022) Binary combinatorial scanning reveals potent poly-alanine-substituted inhibitors of protein-protein interactions. Commun Chem 5:Article number 128.

## Acknowledgements

This work was supported by BBSRC grants BB/N015274/1 and BB/X008215/1 to MG, a BBSRC studentship to AC, and MRC grant MR/T002506/1 to MF. We are grateful for the support of Nikos Pinotsis in the ISMB Protein Crystallography and Biophysics Centre for assistance with x-ray crystallography and to Ben Tagg for assistance with Python. For the purpose of open access, the author(s) has applied a Creative Commons Attribution (CC BY) license to any Author Accepted Manuscript version arising from this submission.

## Author Contributions

J.Z., A.J.C, M.F. and M.G. designed research; J.Z., A.J.C., D.S., T.C. and M.G. performed research; J.Z., A.J.C., D.S., M.F. and M.G. analyzed data; M.G. wrote the paper with input from all of the authors.

## Figure Legends

**Figure 1. Basal interaction of CaMKIIα AA with α-actinin-2 is elevated.** (a) Topologies of CaMKIIα and α-actinin-2 highlighting location of putative regulatory threonines at CaMKII positions 305/306. Panels (b) and (c) show anti-GFP immunofluorescence (left column) and anti-V5/anti-FLAG PLA puncta (middle column) in primary hippocampal neurons expressing GFP and FLAG-α-actinin-2 with either V5-CaMKIIα WT (b) or AA (c). In both cases imaging was performed either before (upper rows) or two hours after (lower rows) chem-LTP. Scale bars are 20 $\mu$m (square panels) and 2 $\mu$m (dendrite close-ups). (d) Quantitation of anti-FLAG/anti-V5 PLA puncta per 10 $\mu$m dendrite before (blue) and after (green) chem-LTP in neurons expressing different CaMKII/actinin pairings. Data are presented as the mean ± standard error (SE). The number of neurons analysed for each condition is shown in parentheses with data collected from three independent cultures for all conditions. In panel d, data were analyzed using an unpaired two-tailed Student's t-test (***P < 0.001).

**Figure 2. Effect of CaMKIIα AA on spine morphology**. (a) GFP imaging of dendrites in primary hippocampal neurons transfected with different combinations of pIRES2-GFP vectors expressing FLAG-α-actinin-2 or V5-CaMKIIα variants. Stubby (red), thin (orange), and mushroom (green) type spines are highlighted with arrows. Scale bars correspond to 2 $\mu$m. Panel (b) shows quantification of spine types across the three conditions either before (upper row) or after (lower row) chem-LTP. Data are presented as mean ± SE spines per 10 $\mu$m dendritic length. Panels c and d show the total spine density and mean spine head diameter for the same five conditions in either naïve synapses (blue) or after chem-LTP (green). The number of neurons analysed for each condition is shown in parentheses. Neurons were imaged deriving from three independent

cultures for each condition. Data were compared using unpaired two-tailed Student's t-tests (***P < 0.001).

**Figure 3. mEPSC recordings from primary hippocampal neurons**. (a) Data from untransfected neurons (top row) or neurons transfected with either V5-CaMKIIα WT (middle row) or AA (bottom row). *Left*: Traces from three representative cells. *Middle*: the corresponding average mEPSC from each cell and the global average mEPSC (± SD, shaded) for each condition (untransfected, gray; V5-CaMKIIα WT, orange; V5-CaMKIIα AA, green). *Right*: Normalized cumulative probability plots of the amplitudes ($\log_{10}$ scale) for each group, with distributions from individual cells shown together with global averaged distributions (dark traces). The plots highlight the wide range within each group and the absence of marked differences between groups. (b) Cumming estimation plot for average mEPSC amplitudes (at −60 mV). The upper panel shows swarmplots with corresponding means and SDs indicated by gapped error bars. In the lower panel unpaired mean differences (upMD) from the untransfected condition are depicted as dots and each bootstrapped 95% confidence interval is indicated by the ends of the vertical error bars. (c) Same as b, but for mEPSC frequency.

**Figure 4. α-actinin-2 binds tightly to a CaMKIIα AA construct spanning residues 1-315**. Panels a-c show representative isotherms for binding of α-actinin-2 EF3-4 to Trx-CaMKIIα (1-315) constructs bearing either T305A (a), T306A (b), or T305A/T306A (c) substitutions. Panels d-f show isotherms for binding of EF3-4 to CaMKIIα (294-315) peptides containing either T305A (d), T306A (e), or T305A/T306A (f) substitutions. For ITC data, top sub-panels show the raw power outputs over time (µcal/s); the bottom sub-panels show the integrated heat changes including a line of best fit to a single site binding model. The final two panels show CaM-dependence of

syntide-2 phosphorylation with either WT (g) or AA (h) CaMKIIα. Each data-point corresponds to the average of two measurements. Comparison of activation with 1 μM CaM (purple) or EF3-4 (orange) is also shown (n=4). Stated $K_d$ and $EC_{50}$ values are mean ± SE. ND = not determined.

**Figure 5. Crystal structure of complex between α-actinin-2 EF3-4 and CaMKIIα AA**. (a) Coomassie gel showing elution of a mixture of CaMKIIα 1-315 AA and a molar excess of α-actinin-2 EF3-4 from a Superdex 75 size exclusion column. The earlier fractions containing the complex were used for crystallization. (b) Overview of the structure obtained following crystallization with $Mg^{2+}$/ADP (PDB ID 7B57). The kinase domain and regulatory segment of CaMKIIα are shown in green and blue, respectively; EF3-4 is colored orange. Panels c and d show two close-up views of the core interface related by a 90° rotation, with α-actinin-2 residues in orange and CaMKII residues in blue.

**Figure 6. Comparison of regulatory segment binding modes**. Panels a to c show equivalent views of the CaMKIIα regulatory segment (blue) highlighting the relative binding orientations of CaM (a) and EF3-4 (b) to WT regulatory segment, and EF3-4 to the AA variant (c) observed in structures 2WEL, 6TS3 and 7B57, respectively. The CaM N-lobe is coloured purple; the C-lobe is violet. For α-actinin-2, EF3 is coloured light orange; EF4 is olive. (d) Alignment of CaMKII regulatory segment Cα positions taken from the three structures determined in this study and from the WT CaMKIIα regulatory segment – EF3-4 complex (6TS3). The conformation of the segment is highly similar within 0.6 Å RMSD for all pairwise alignments of positions that are visible across all four structures (294-308). (e) Superposition of EF3-4 taken from the structure in complex with WT CaMKIIα regulatory segment (grey) onto the complex with the AA variant, in which EF3-4 is coloured orange.

**Figure 7. Molecular basis of enhanced α-actinin-2 binding to CaMKIIα AA**. (a) View of the CaMKIIα AA – EF3-4 complex (PDB ID 7B57) highlighting the separation of EF3-4 and the CaMKII kinase domain: the two do not engage in any direct interactions. Panels b and c show close-up views of the EF3-4 – CaMKIIα AA interface highlighting interactions in the vicinity of A305/A306 (b), and interactions involving K291/K292 (c). Panels d and e show representative isotherms for binding of α–actinin-2 EF3-4 to either the WT (d) or AA (e) variants of CaMKIIα 290-309. The top sub-panels show the raw power output (μcal/s) over time; the bottom sub-panels show the integrated data including a line of best fit to a single site binding model. Stated $K_d$ values are averages from three replicates.

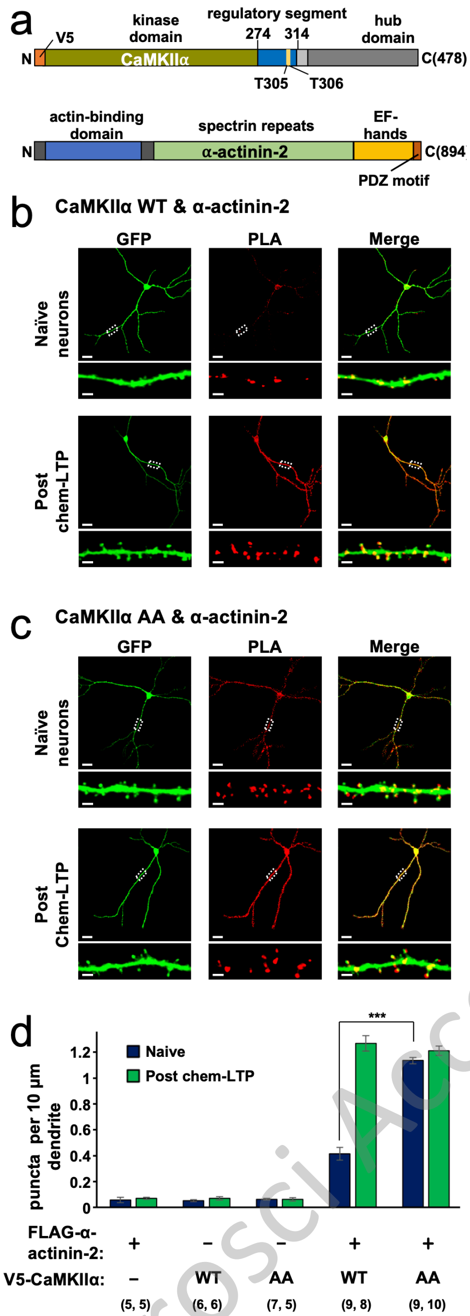
a
V5
kinase domain
regulatory segment
274
314
hub domain
N
CaMKIIα
C(478)
T305
T306
actin-binding domain
spectrin repeats
EF-hands
N
α-actinin-2
C(894
PDZ motif
b
CaMKIIα WT & α-actinin-2
GFP
PLA
Merge
Naïve neurons
Post chem-LTP
c
CaMKIIα AA & α-actinin-2
GFP
PLA
Merge
Naïve neurons
Post Chem-LTP
d
Naive
Post chem-LTP
***
puncta per 10 µm dendrite
FLAG-α-actinin-2:
V5-CaMKIIα:
(5, 5)
(6, 6)
(7, 5)
(9, 8)
(9, 10)

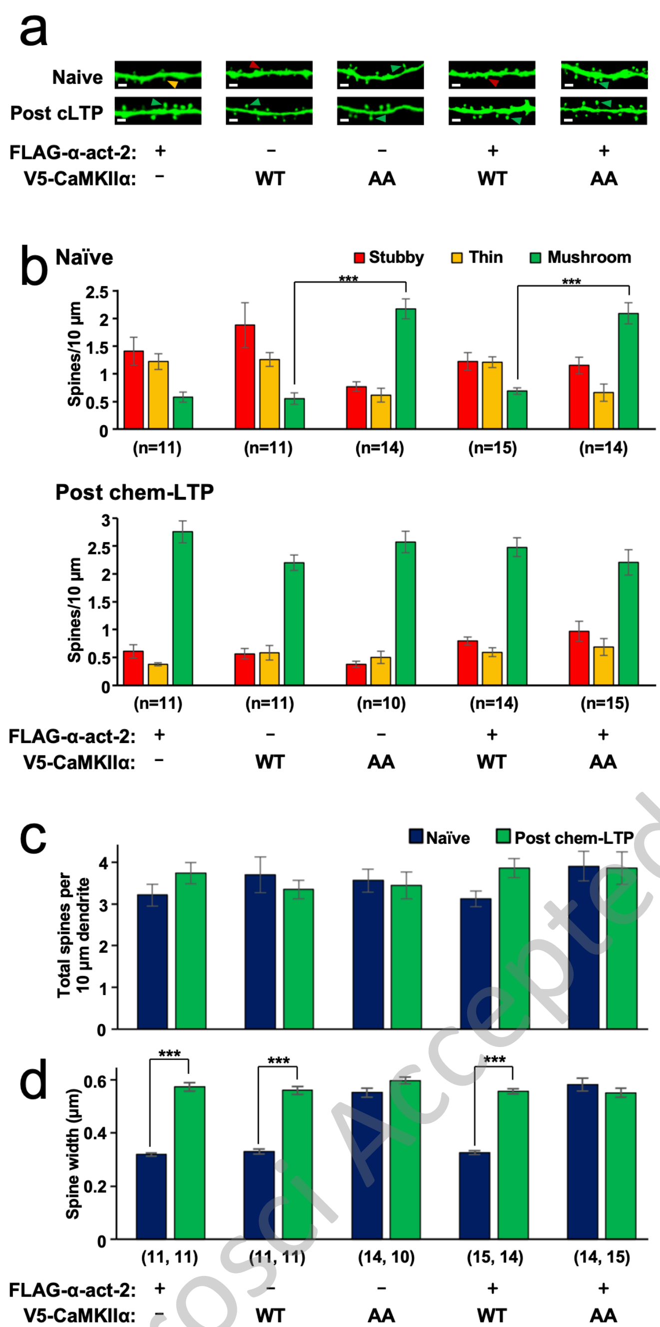
a
Naive
Post cLTP
FLAG-α-act-2: + – – + +
V5-CaMKIIα: – WT AA WT AA
b Naïve
Stubby Thin Mushroom
***
***
Spines/10 μm
2.5
2
1.5
1
0.5
0
(n=11) (n=11) (n=14) (n=15) (n=14)
Post chem-LTP
Spines/10 μm
3
2.5
2
1.5
1
0.5
0
(n=11) (n=11) (n=10) (n=14) (n=15)
FLAG-α-act-2: + – – + +
V5-CaMKIIα: – WT AA WT AA
c
Naïve Post chem-LTP
Total spines per 10 μm dendrite
4
3
2
1
0
d
***
***
***
Spine width (μm)
0.6
0.4
0.2
0
(11, 11) (11, 11) (14, 10) (15, 14) (14, 15)
FLAG-α-act-2: + – – + +
V5-CaMKIIα: – WT AA WT AA

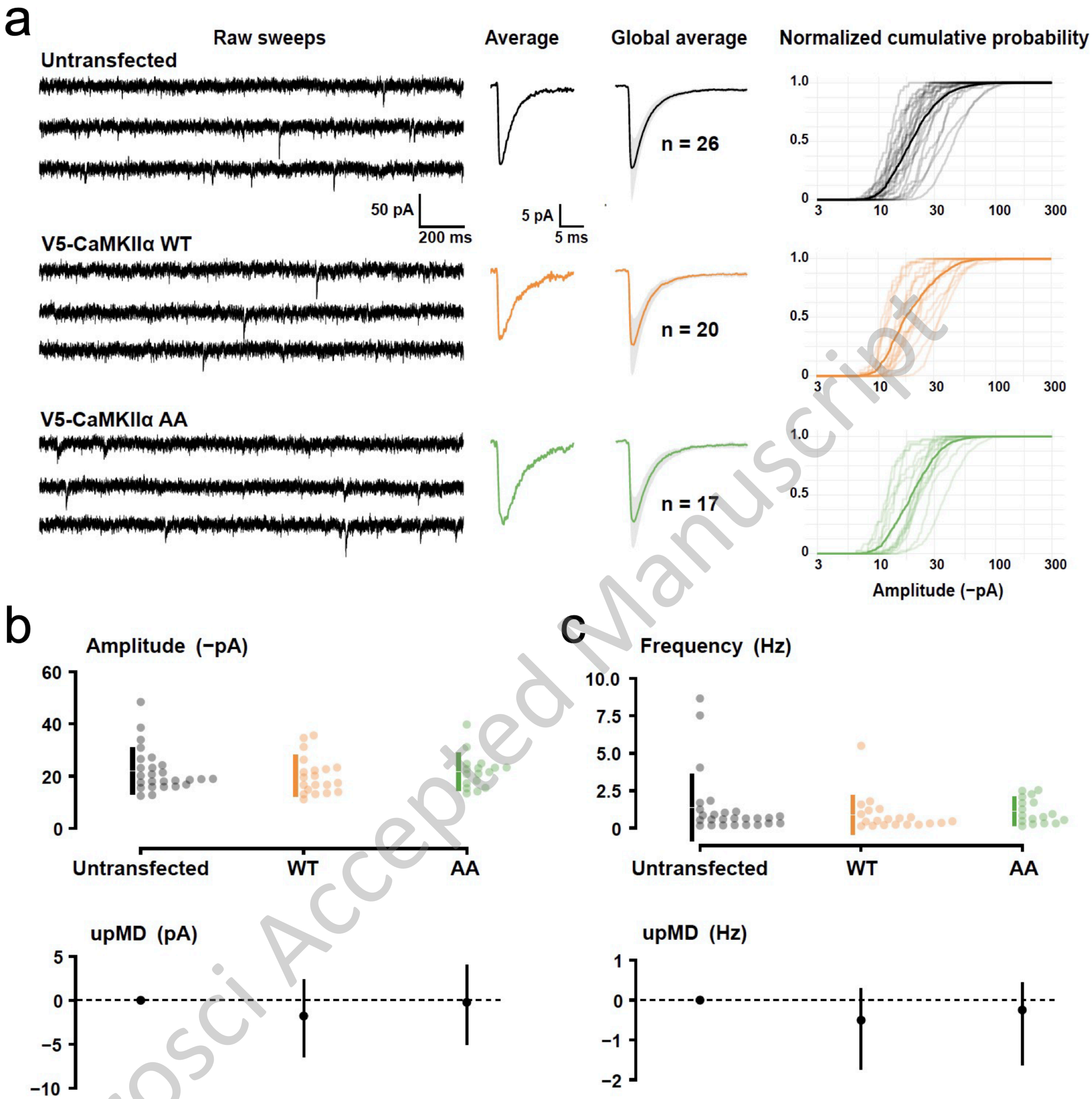

a
Raw sweeps
Average
Global average
Normalized cumulative probability
Untransfected
50 pA
200 ms
5 pA
5 ms
n = 26
V5-CaMKIIα WT
n = 20
V5-CaMKIIα AA
n = 17
Amplitude (−pA)
b
Amplitude (−pA)
Untransfected
WT
AA
upMD (pA)
c
Frequency (Hz)
Untransfected
WT
AA
upMD (Hz)

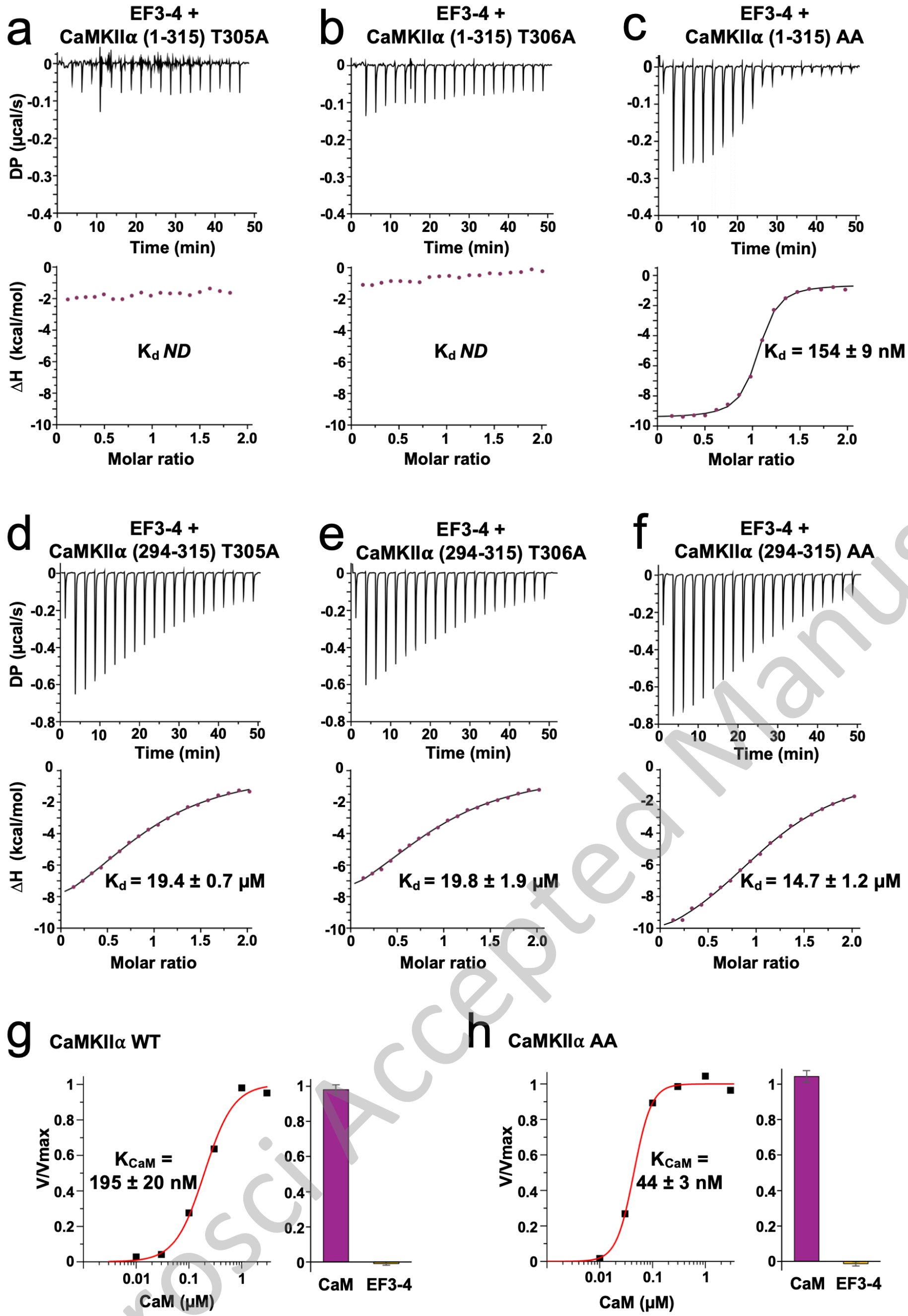
a
EF3-4 +
CaMKIIα (1-315) T305A
DP (µcal/s)
Time (min)
ΔH (kcal/mol)
Kd ND
Molar ratio
b
EF3-4 +
CaMKIIα (1-315) T306A
Kd ND
c
EF3-4 +
CaMKIIα (1-315) AA
Kd = 154 ± 9 nM
d
EF3-4 +
CaMKIIα (294-315) T305A
Kd = 19.4 ± 0.7 µM
e
EF3-4 +
CaMKIIα (294-315) T306A
Kd = 19.8 ± 1.9 µM
f
EF3-4 +
CaMKIIα (294-315) AA
Kd = 14.7 ± 1.2 µM
g
CaMKIIα WT
V/Vmax
KCaM =
195 ± 20 nM
CaM (µM)
CaM
EF3-4
h
CaMKIIα AA
KCaM =
44 ± 3 nM

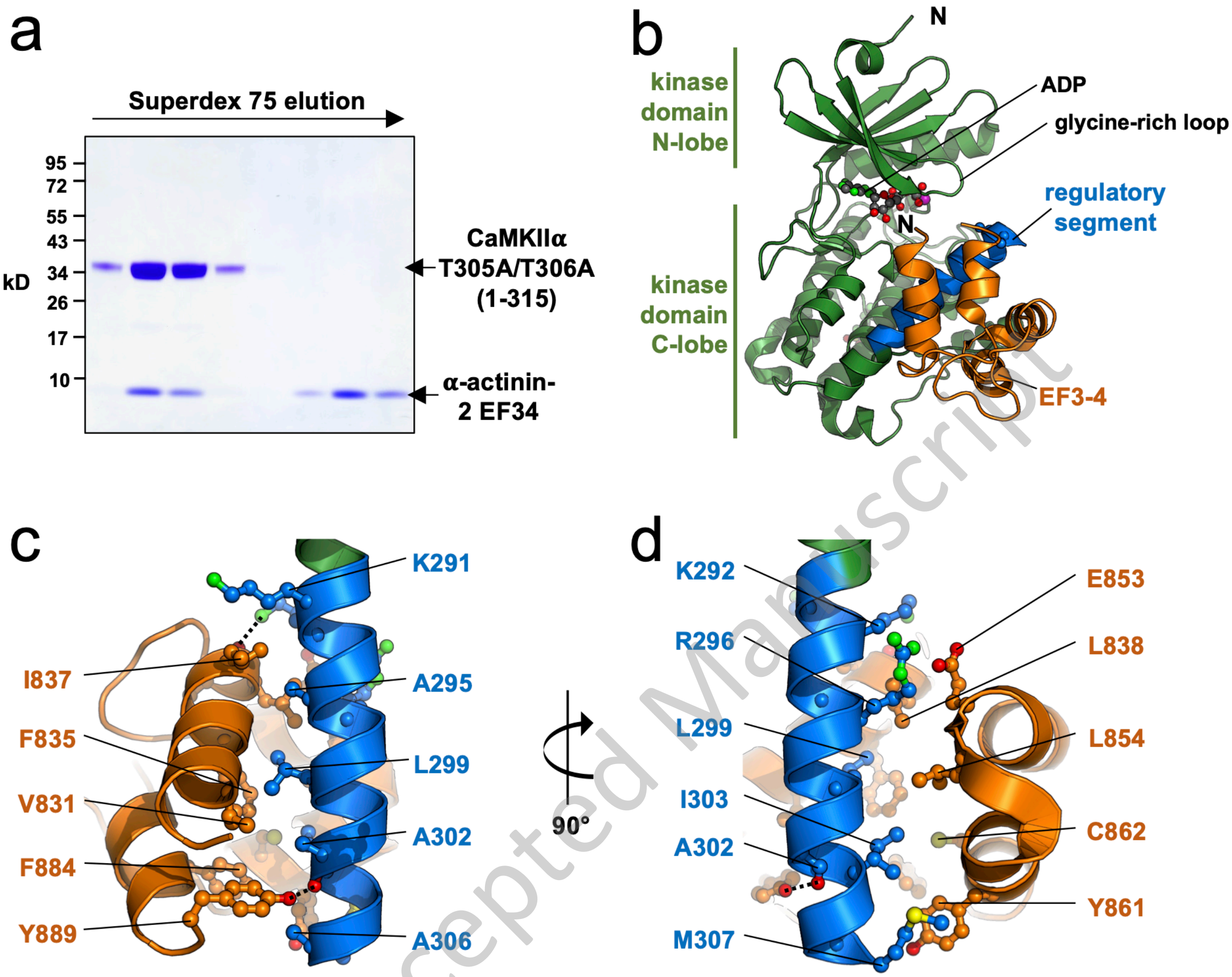
a
Superdex 75 elution
95
72
55
43
34
26
17
10
kD
CaMKIIα T305A/T306A (1-315)
α-actinin-2 EF34
b
N
ADP
glycine-rich loop
kinase domain N-lobe
regulatory segment
N
kinase domain C-lobe
EF3-4
c
K291
I837
A295
F835
L299
V831
A302
F884
Y889
A306
90°
d
K292
E853
R296
L838
L299
L854
I303
C862
A302
Y861
M307

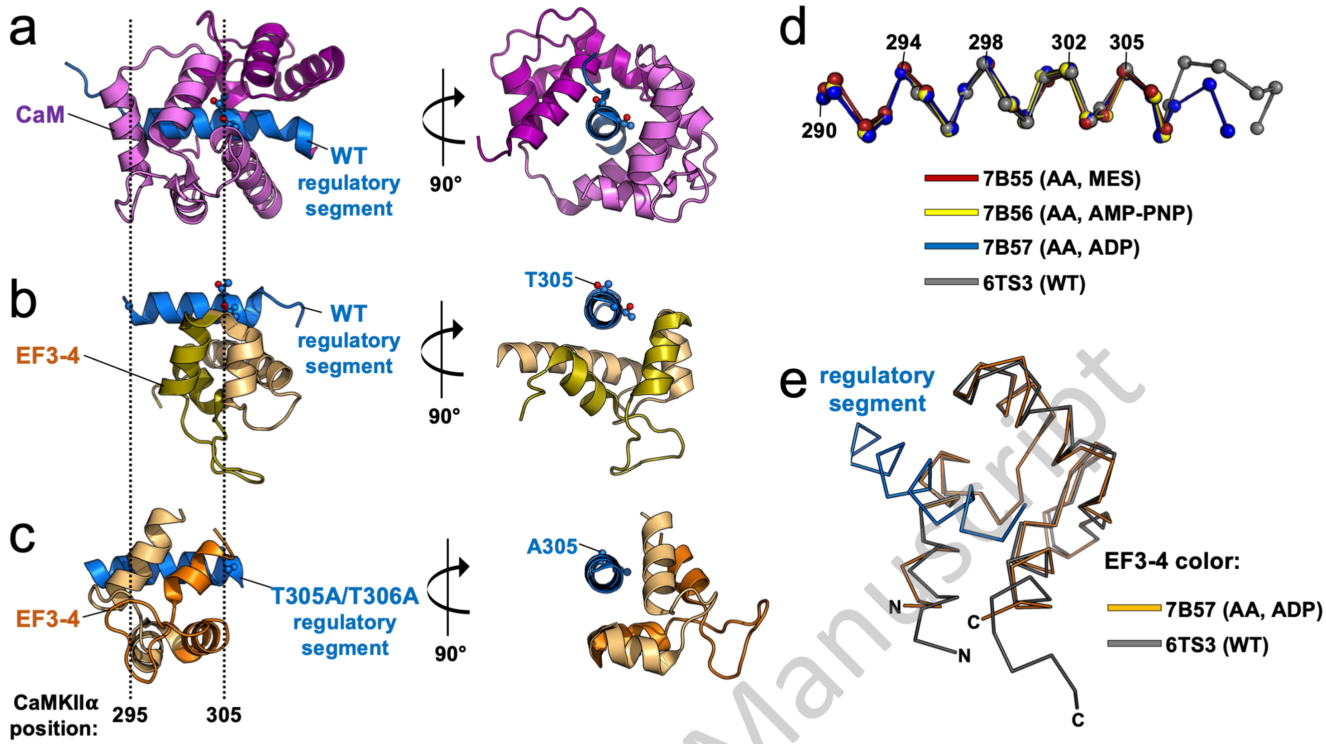

a
CaM
WT
regulatory
segment
90°
b
EF3-4
WT
regulatory
segment
90°
T305
c
EF3-4
T305A/T306A
regulatory
segment
90°
A305
CaMKIIα
position:
295
305
d
294
298
302
305
290
7B55 (AA, MES)
7B56 (AA, AMP-PNP)
7B57 (AA, ADP)
6TS3 (WT)
e
regulatory
segment
EF3-4 color:
7B57 (AA, ADP)
6TS3 (WT)
N
C
N
C

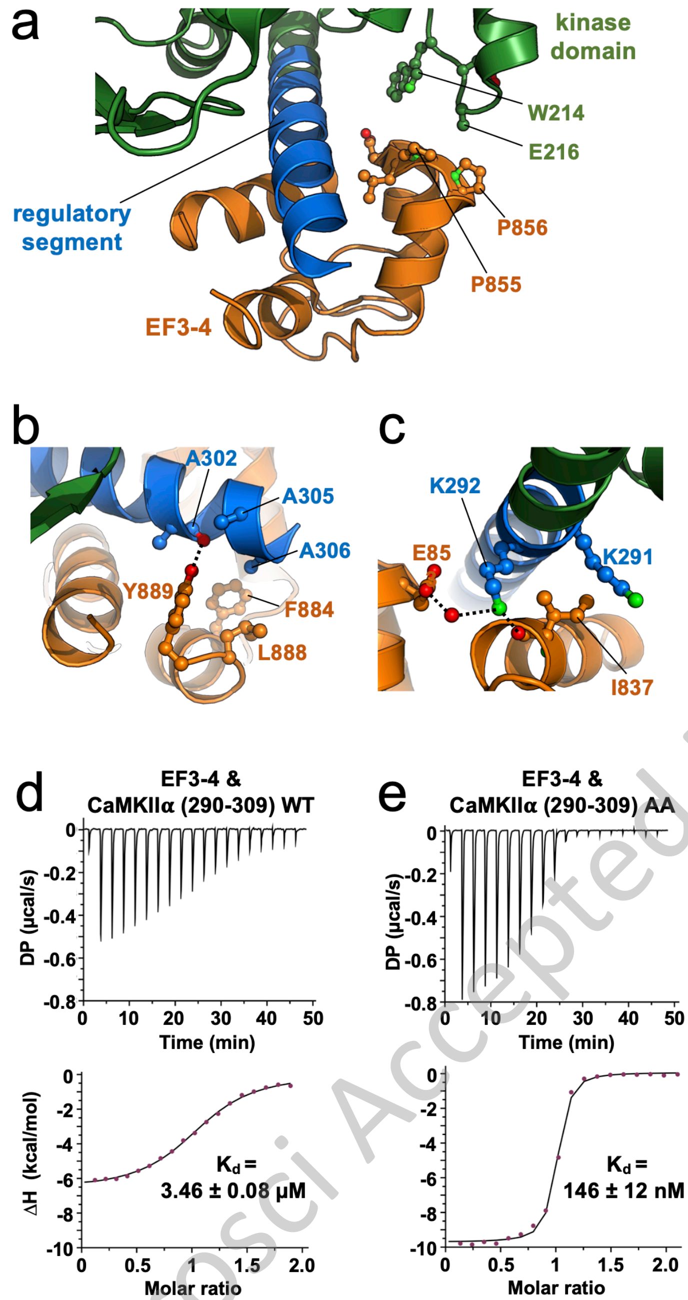

a
kinase domain
W214
E216
regulatory segment
P856
P855
EF3-4
b
A302
A305
A306
Y889
F884
L888
c
K292
E85
K291
I837
d
EF3-4 & CaMKIIα (290-309) WT
DP (µcal/s)
Time (min)
ΔH (kcal/mol)
Kd = 3.46 ± 0.08 µM
Molar ratio
e
EF3-4 & CaMKIIα (290-309) AA
DP (µcal/s)
Time (min)
Kd = 146 ± 12 nM
Molar ratio